Journal of Materials Chemistry A

ROYAL SOCIETY OF CHEMISTRY

PAPER

View Article Online
View Journal

Cite this: DOI: 10.1039/d5ta07225e

Towards sustainable biogas upgrading: MIL-120(Al) as a cost-effective water stable MOF for CO_2/CH_4 separation

Marta Bordonhos, [ab] Rosana Vieira Pinto, [c] Tânia Frade,[a] Bingbing Chen,[c] Farid Nouar,[c] Georges Mouchaham, [c] José R. B. Gomes, [b] Christian Serre[c] and Moisés Luzia Pinto *[a]

The microporous MIL-120(Al) MOF has been tested for CO_2/CH_4 separation. The material has been synthesised in powder form at the kilogram scale and shaped into spherical beads without significant loss in adsorption capacity (on average, *ca.* 7% for CO_2). MIL-120(Al) is more selective towards CO_2 (IAST mean selectivity of 10.6–35 between 0.1–10 bar), showing a good adsorption capacity and a moderate enthalpy of adsorption (−36.7 to −39.1 kJ mol^{-1} in the low loading regime). Molecular simulation studies have revealed a probable rotation of the μ_2-OH groups with increasing CO_2 pressure altering the CO_2 adsorption capacity at higher pressures. Breakthrough experiments have confirmed the CO_2/CH_4 selectivity of MIL-120(Al) and have shown that the material can retain its original adsorption separation performance after regeneration, following consecutive cycles (10 cycles) and prolonged exposure to high amounts of water vapour, demonstrating the potential of this MOF for biogas upgrading.

Received 4th September 2025
Accepted 8th February 2026

DOI: 10.1039/d5ta07225e

rsc.li/materials-a

Introduction

Over the last years, the demand for sustainable energy sources has been growing, driving intensified research into biogas upgrading, a critical process to enhance methane (CH_4) purity in raw biogas by removing carbon dioxide (CO_2). Biogas is a renewable energy source that originates from the anaerobic digestion of organic matter and can serve as a substitute for fossil natural gas. However, raw biogas can typically contain up to 50% (V/V) in CO_2, along with other contaminants and trace impurities such as hydrogen sulphide (H_2S) and moisture, which lower its energy value and limit its direct use in conventional energy grids or as fuel. To maximise its utility, efficient CO_2 separation is essential to obtain biomethane with a high CH_4 molar content (>96%), making it comparable to conventional natural gas.[1,2]

Various technologies have been explored for CO_2/CH_4 separation in biogas upgrading, including absorption, adsorption, and membrane separation.[1,2] Among these, adsorption-based cyclic processes using porous materials, like pressure swing adsorption (PSA), have garnered significant attention due to their potential for energy-efficient and cost-effective separations. Metal–organic frameworks (MOFs), crystalline micro- or mesoporous hybrid solids, with their high surface area, tuneable pore structures, and selective gas adsorption properties, have emerged as promising candidates for this application.[3,4] However, many MOFs suffer from hydrothermal and/or acid–base instability, complex synthesis routes, and high production costs, limiting their large-scale implementation.[5,6] MIL-120(Al),[7] an aluminium-based ultramicroporous MOF, emerges as a promising alternative for biogas upgrading due to its high stability toward coordinating and corrosive gases, such as water, NO_x or SO_x.[8] MIL-120(Al) is among the most cost-effective adsorbent materials, with an estimated production cost of approximately 13 \$ kg^{-1} and a scalable synthesis protocol.[8] Moreover, it exhibits excellent CO_2 adsorption capacity up to 1 bar,[8] enabling more energy-efficient separation processes. Herein, we investigate the CO_2/CH_4 separation performance of MIL-120(Al) in the context of biogas upgrading (Fig. 1) from a combination of single-component adsorption experiments and molecular simulations up to 10 bar, and gas mixture breakthrough experiments at *ca.* 1 bar. These allowed the assessment of its adsorption capacity, pore structure, behaviour under dry and wet conditions, selectivity and recyclability, while benchmarking its performance against other adsorbent materials. MIL-120(Al) demonstrates a remarkable potential for industrial biogas purification, offering a breakthrough solution to the pressing challenges of economic scalability and operational feasibility in sustainable energy applications.

[a]*CERENA, Departamento de Engenharia Química, Instituto Superior Técnico, Universidade de Lisboa, Av. Rovisco Pais, No. 1, 1049-001 Lisboa, Portugal. E-mail: moises.pinto@tecnico.ulisboa.pt*

[b]*CICECO – Aveiro Institute of Materials, Department of Chemistry, University of Aveiro, Campus Universitário de Santiago, 3810-193 Aveiro, Portugal*

[c]*Institut des Matériaux Poreux de Paris (IMAP), ESPCI Paris, École Normale Supérieure de Paris, CNRS, PSL University, 75005 Paris, France*

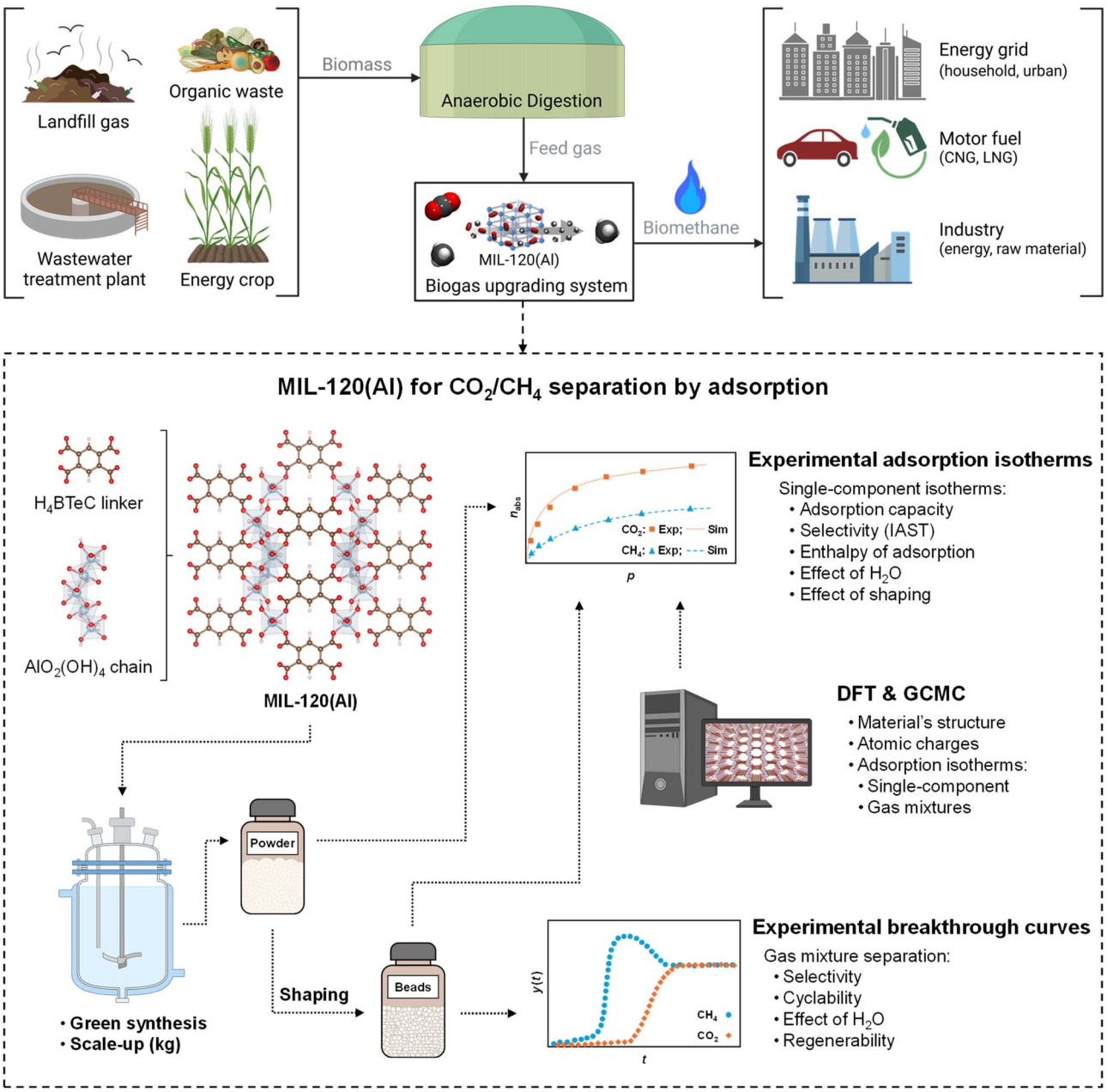

Fig. 1 The study developed in this work for the investigation of MIL-120(Al) for CO_2/CH_4 separation in the context of biogas upgrading. Figure partially created in BioRender. Pinto, R. (2026) https://BioRender.com/w47s435.

Results and discussion

Adsorption performance under dry conditions

MIL-120(Al) has been synthesised at the kilogram scale using an environmentally friendly, scalable and high-yield synthesis method, following a previous protocol developed by some of us.[8] The characterisation details, provided in Section S1 in the SI, confirm the structural integrity, porosity and thermal stability of the material. Single-component CO_2 and CH_4 adsorption isotherms measured at 25 °C for the powder form of MIL-120(Al) are represented in Fig. 2A. Additional details are described in the Experimental section and in Section S2.A in the SI. The experimental data and corresponding isotherm model fittings are reported in Tables S2 and S3 in the SI. As expected, MIL-120(Al) shows a higher adsorption capacity for CO_2 than for CH_4 in the entire pressure range studied, suggesting the potential of this MOF for biogas upgrading. In comparison with other adsorbent materials (additional details in Section S2.D in the SI), the CO_2 uptake of MIL-120(Al) at 1 bar, *ca.* 3.6 mmol g^{-1}, is higher than for the reviewed activated carbons[9–12] (AC), carbon molecular sieves[13,14] (CMS), pillared clays,[15] silica-based materials,[16–18] and periodic mesoporous organosilicas[19] (PMO). MIL-120(Al) also shows a higher or similar CO_2 uptake at 1 bar than the other MOFs reviewed in the SI,[13,20–23] with the exception

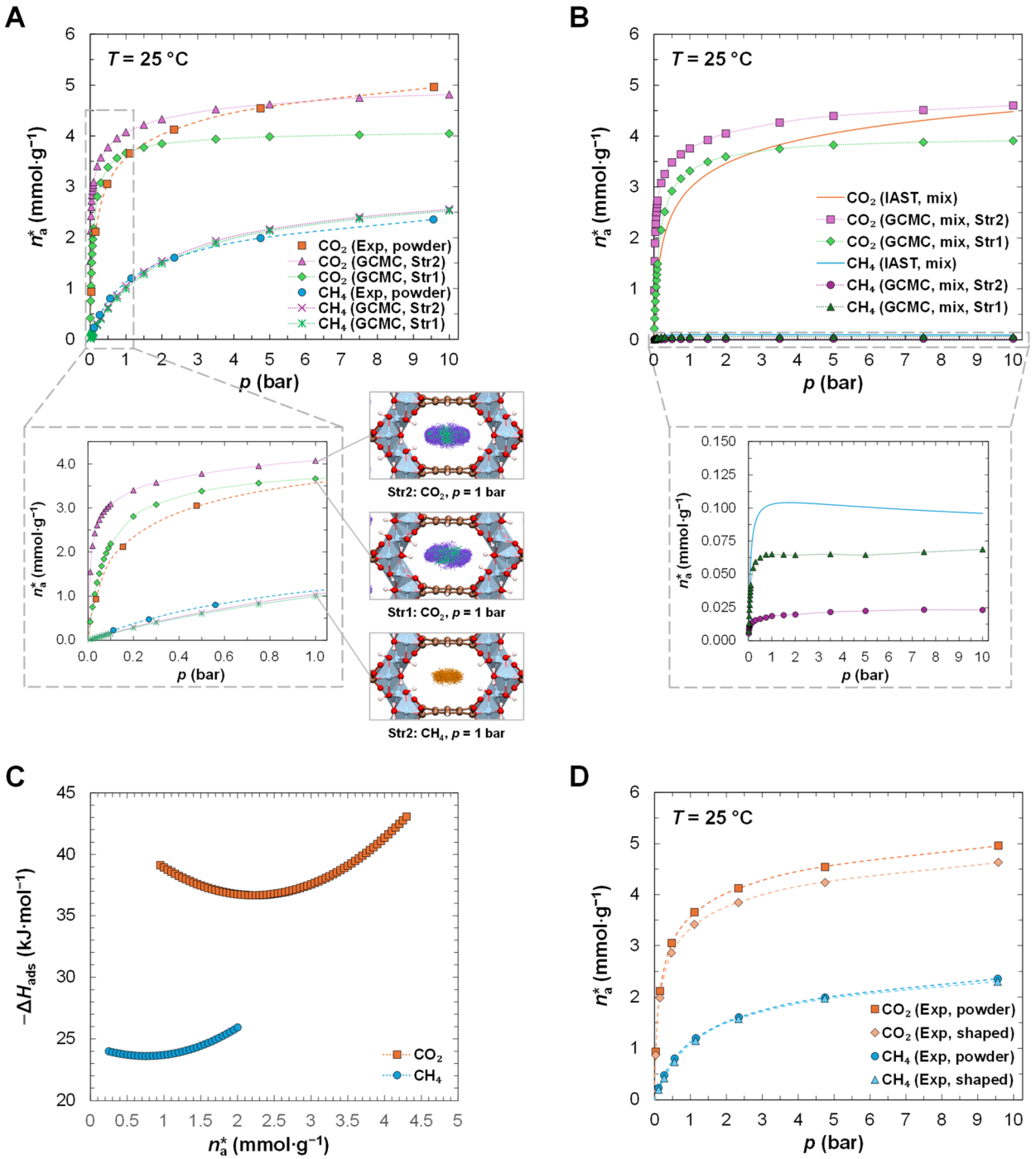

Fig. 2 (A) Single-component adsorption isotherms of CO_2 and CH_4 at 25 °C measured for the powder form of MIL-120(Al) and calculated by GCMC for Str2 and Str1, and density plots generated from GCMC simulations for the single-component adsorption at 1 bar of CO_2 in Str2 and Str1 and of CH_4 in Str2; (B) mixture isotherms calculated by IAST and GCMC (Str2 and Str1) for a binary CO_2 : CH_4 mixture with % (V/V) = (50 : 50)%; (C) isosteric enthalpy of adsorption (ΔH_{ads}) calculated from the Clausius–Clapeyron equation from the single-component experimental data measured at 25, 35 and 45 °C; (D) comparison of the single-component adsorption isotherms of CO_2 and CH_4 at 25 °C measured for the powder and shaped forms of MIL-120(Al). All isotherms are reported in absolute adsorbed amounts, n_a^*. The dashed lines in (A) and (D) represent the non-linear least-squares fit of the isotherm model to the experimental data (*cf.* Table S3 in the SI). The dotted lines in (A), (B) and (C) serve only as a visual guide of the data trends to the reader. The density maps in (A) were generated from the combined snapshots of GCMC simulations collected every 100 cycles of the production run. Colour code for framework atoms in the density maps: carbon (C, brown); hydrogen (H, white); oxygen (O, red); aluminium (Al, blue). Colour code for CO_2 atoms in the density maps: C (green); O (violet). Colour code for the C atoms from CH_4 (UA) in the density maps: C (orange). CO_2 and CH_4 (UA) atoms were drawn without bonds (where applicable) and on a 1 : 8 radii scale relative to framework atoms in the density maps. Structure drawing and density maps produced by VMD 1.9.4.[36]

of MIL-160(Al) (as a powder)[24] and CuBTC.[13] In comparison with zeolites,[13,25–30] MIL-120(Al) shows a mixed uptake performance: higher than some, including zeolites beta,[25] 5A [28] and Na-ZSM-5,[30] but lower than zeolites 13X [26])/NaX,[13] 4A [27] and NaY.[29]

Grand-canonical Monte Carlo (GCMC) simulations have been run in RASPA 2.0,[31] at 25, 35 and 45 °C and up to 10 bar, and contemplated two different structures for MIL-120(Al), Str2 (Fig. S7 in the SI) and Str1 (Fig. S8 in the SI), in accordance with the strategy and nomenclature employed in a previous work by our colleagues up to 1 bar.[8] The models of these two structures differ mainly in the position of eight H atoms of the μ_2-OH groups in the unit cell (four different pairs of H atoms) and have been optimised by density functional theory (DFT) in VASP[32–35] 6.1.2. Additional details can be found in the Experimental section and in Section S2.B in the SI. Regarding CO_2 adsorption, Str2 presents higher uptakes than Str1. In MIL-120(Al), CO_2 interacts preferentially with the μ_2-OH groups of the metal clusters[8] on both sides of the pore, as can be seen in the density maps (25 °C, 1 bar) in Fig. 2A, and in greater detail for 0.01, 0.1, 1 and 10 bar in Fig. 3. The CO_2 density maps at 25 °C are also represented for the full simulation box in the SI in Fig. S9 to S16 for Str2, and S21 to S28 for Str1. The interaction of CO_2 with these μ_2-OH groups is likely due to the quadrupole moment of

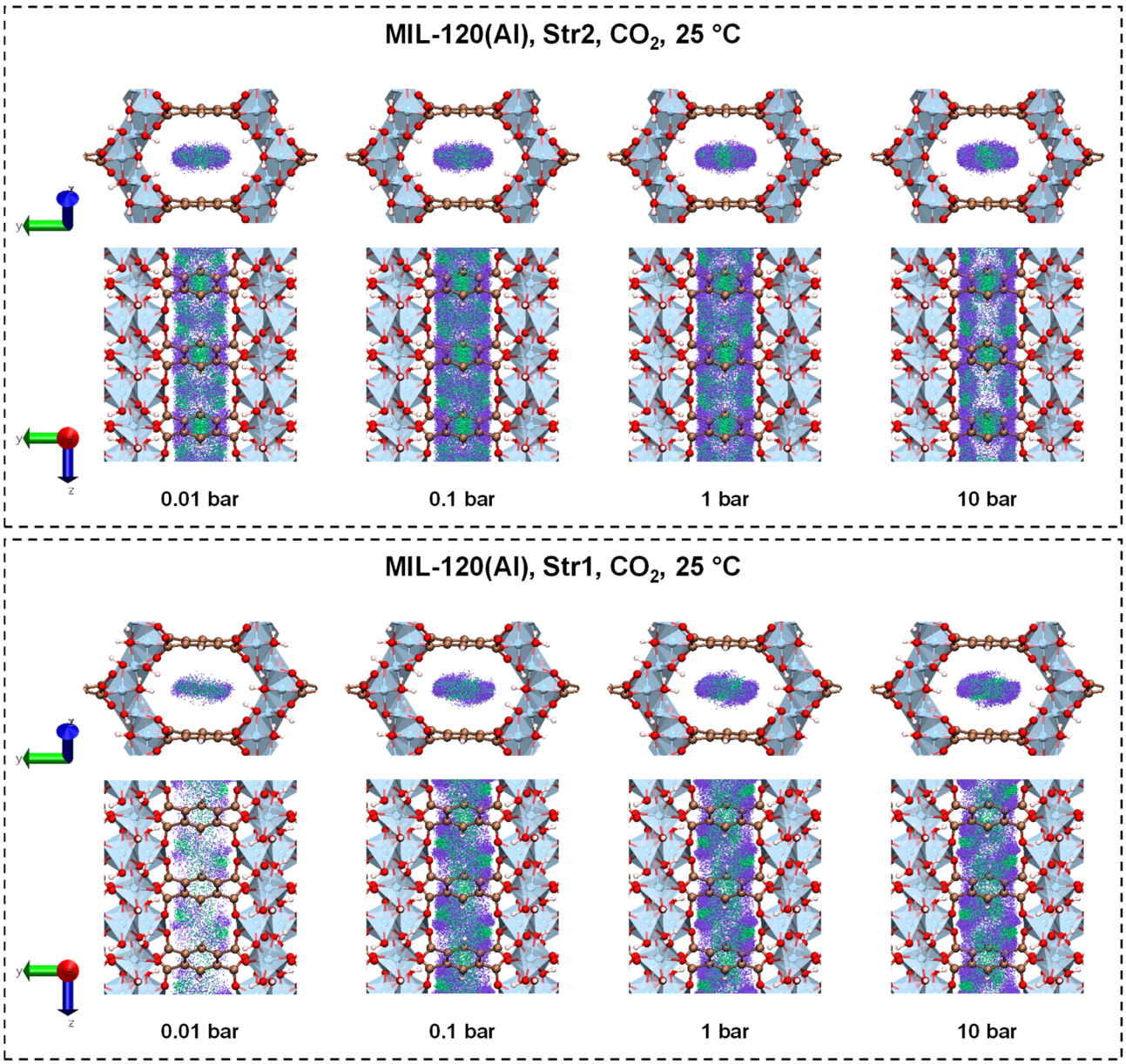

Fig. 3 Density maps of the single-component adsorption of CO_2 at 25 °C and 0.01, 0.1, 1 and 10 bar obtained for Str2 (top) and Str1 (bottom) from GCMC calculations, as viewed from two directions. For the complete set of density maps, the reader is referred to Section S2.B in the SI. Colour code for framework atoms: C (brown); H (white); O (red); Al (blue). Colour code for CO_2 atoms: C (green); O (violet). CO_2 atoms are drawn without bonds and on a 1 : 8 radii scale relative to framework atoms. Density maps generated from the combined snapshots of GCMC simulations collected every 100 cycles of the production run. Structure drawing and density maps produced by VMD 1.9.4.[36]

CO_2, that leads to strong electrostatic interactions between the O atoms in CO_2 and the H atoms in the μ_2-OH groups.

As the orientation of some of these groups in Str2 and Str1 is different, the resulting CO_2 isotherms are different, as also verified and discussed by our colleagues in a previous work.[8] The predicted Str1 isotherm more closely resembles the experimental isotherm until *ca*. 1 bar. The small differences observed until 1 bar between this work and the previous study can be attributed to both the experimental pore volume, *ca*. 0.28 $cm^3\ g^{-1}$ in Chen *et al.*[8] (value converted from Fig. S1D for MIL-120-AP powder for $p/p^\circ \approx 0.83$) *vs.* 0.21 $cm^3\ g^{-1}$ (for $p/p^\circ \approx 0.85$, *cf.* Table S1 in the SI) in this work that can be due to minor structural differences in the synthesised materials, and the volume of the crystallographic unit cells of the simulated structures, *ca*. 1030 $Å^3$ for Str1 and *ca*. 1056 $Å^3$ for Str2 in Chen *et al.*[8] (values reported originally for the primitive cell, *i.e.*, half of the total volume of the unit cell) *vs. ca*. 1045 $Å^3$ (for the unit cell, *cf.* Tables S4 and S5 in the SI) for both structures in this work. As pressure increases, the trend of the experimental isotherm starts deviating from Str1 and moving towards Str2, following Str2 more closely from 5 bar onwards, as can be seen more clearly in the semi-logarithmic plot of the isotherms in Fig. 4. This indicates that there is probably a rotation of the μ_2-OH groups as pressure increases, and neither Str1 nor Str2 can fully represent CO_2 adsorption on MIL-120(Al) on their own. As such, we suspect that the real structure can be seen as a composite of not only Str1 and Str2 but also of other structures with other orientations of the μ_2-OH groups, highlighting the hydroxyl rotational flexibility of this framework. Indeed, this flexibility has recently attracted scientific attention and is currently being investigated with machine learning potentials by different research groups.[37,38] For the adsorption of CH_4 there is no noticeable difference between Str2 and Str1. This is because CH_4 does not have a quadrupole moment that can induce strong (electrostatic) interactions with the μ_2-OH groups, thus it is less sensitive to their orientation, unlike CO_2. Its lower uptake is mostly due to weaker van der Waals interactions with the chemical environment inside the pores, that are the same for both types of structures. In comparison with the experimental CH_4 isotherm at 25 °C, there is only a minor increase in CH_4 uptake from *ca*. 2 bar onwards in the simulated isotherms, that is acceptable within the uncertainty of both methods. Looking into the density of gas inside the pores at 25 °C, the increase in CO_2 and CH_4 density from 0.01, to 0.1, to 1, to 10 bar in Str2 and Str1 can be seen in greater detail from two directions in Fig. 3 (only CO_2) and in Fig. S9 to S32 in the SI.

Complementary radial distribution functions (RDFs) for the interaction of each framework atom-type of Str2 (Table S7 in the SI) and Str1 (Table S8 in the SI) with the C or O atoms of CO_2 at 25 °C have also been computed in RASPA[31] and are plotted for the same pressures in Fig. S33 to S46 in the SI. Interestingly, for CO_2 adsorption in Str2, where the pore-facing μ_2-OH groups are oriented toward the same plane inside the pore channel (*cf.* Table S4 and Fig. S7 in the SI), it can be seen in the density maps in Fig. 3, top, that CO_2 molecules align both perpendicularly and axially to the pore channel length, as observed previously,[8] and that as pressure increases more CO_2 molecules start adsorbing axially to the pore channel length and slightly closer to the metal chain on the side wall of the pore, resulting in a rectangle-like shape of adsorbed CO_2 molecules along the length of the pore channel (*cf.* Fig. 3, top). In the RDF plots in Fig. S33 to S36 in the SI, it can be seen in general that the intensity of some of the first RDF peaks between CO_2 atoms and framework atom-types increases from lower to higher pressures. This can be attributed to the increase in CO_2 density inside the pores, that leads to a closer (denser) and more ordered packing of the CO_2 molecules (*cf.* Fig. 3, top). It should be noted that RDF peaks at distances greater than 5–6 Å can also represent the interaction of adsorbate atoms with framework atoms of neighbouring pores, as the maximum pore dimensions, measured from the centre of mass of framework atoms and without taking into account the van der Waals radii, are *ca*. 7 Å (between the organic linkers at the top and bottom of the unit cell, *cf.* Fig. S7 in the SI) and *ca*. 9.4 Å (between opposite oxygens from the metal clusters with atom-type label 8, *cf.* Fig. S7 and Table S7 in the SI). For Str1 (*cf.* Fig. 3, bottom), where the rotated pore-facing μ_2-OH groups on each side of the pore have different orientations relative to each other (*cf.* Table S5 and Fig. S8 in the SI), CO_2 molecules are adsorbed in alignment with these μ_2-OH groups, but with a higher density along and in parallel to the pore channel (*cf.* Fig. 3, bottom). The RDF plots for this structure, represented in Fig. S37 to S46 in the SI, show, in general, notably higher intensity peaks at 0.01 bar than at higher pressures. This can be due to the highly specific interactions of CO_2 at 0.01 bar, that corresponds to a low loading of *ca*. 0.4 mmol g^{-1} (*cf.* Fig. 4), with the framework atoms that results in a well-defined coordination of this low amount of CO_2 molecules with the adsorption sites inside the pores. At higher pressures, as more CO_2 occupies the available pore space, the molecules are more dispersed, and the intensity of the peaks decreases sharply. This is in contrast with the observations for Str2 (*cf.* Fig. S33 to S36 in the SI), as in Str2 the CO_2 uptake at 0.01 bar is *ca*. 1.5 mmol g^{-1}, and the CO_2 molecules are already more dispersed (*cf.* density maps at 0.01 bar in Fig. 3). Nevertheless, a slight increase in peak intensity can also be seen from 0.1 to 10 bar in some RDFs for Str1, as seen for Str2. For CH_4, the density maps for both structures (*cf.* Fig. S17 to S20 for Str2 and S29 to S32 for Str2 in the SI) show a similar density of adsorbed CH_4 molecules, that is located along and in the middle of the pore channel.

Adsorption isotherms were calculated for an equimolar CO_2 : CH_4 mixture at 25 °C based on the Ideal Adsorbed Solution Theory (IAST),[39,40] from the Virial isotherm model adjusted to the single-component experimental data (*cf.* Tables S2 and S3 in the SI), and by GCMC for Str2 and Str1 (*cf.* Table S6 in the SI). The mixture isotherms, represented in Fig. 2B, show a high selectivity for CO_2 over CH_4, as the mixture uptakes of CO_2 are close to the uptakes of the single-component CO_2 isotherms, whereas for CH_4, the mixture uptakes are much lower (up to two orders of magnitude for Str2) than those of the single-component CH_4 isotherms. The results for CO_2 are consistent with the observations made for its single-component adsorption: the IAST-predicted mixture isotherm is more similar to Str1 at lower pressures and to Str2 at higher pressures. For CH_4,

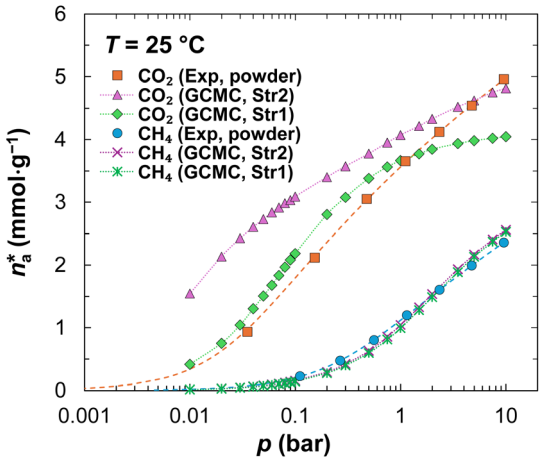

Fig. 4 Semi-logarithmic plot of the CO_2 and CH_4 isotherms (25 °C) represented in Fig. 2A. All isotherms are reported in absolute adsorbed amounts, n_a^*. The dashed lines represent the non-linear least-squares fit of the Virial isotherm model to the experimental data (*cf.* Table S3 in the SI), and the dotted lines serve only as a visual guide of the simulated data trends to the reader.

IAST overestimates its mixture uptake in comparison with the GCMC-calculated uptake for both Str2 and Str1.

The isotherms measured at 35 and 45 °C, represented in Fig. S4 in the SI, show lower gas uptakes with increasing temperature, with lower slopes and an overall similar isotherm shape. The isotherms calculated by GCMC at 35 and 45 °C for Str1 and Str2 show similar trends to those calculated at 25 °C, as can be seen in Fig. S47 in the SI: for CO_2, Str1 and Str2 are closer to the experimental isotherms at lower and higher pressures, respectively, and for CH_4 both Str1 and Str2 follow the experimental isotherms. The isosteric enthalpy of adsorption, ΔH_{ads}, has been calculated from the Clausius–Clapeyron equation[41] using the isotherm fittings from the experimental data for the three temperatures within the same loading range (*cf.* Tables S2 and S3 in the SI). The results are represented in Fig. 2C. CO_2 shows a moderate enthalpy of adsorption, between *ca.* −36.7 and −39.1 kJ mol^{-1} in the lower loading regime (≤3 mmol g^{-1}), and CH_4 shows a lower enthalpy of adsorption, with values between *ca.* −23.6 and −24.0 kJ mol^{-1} in the lower loading regime (≤1.2 mmol g^{-1}). The estimated values for the isosteric enthalpy of adsorption of CO_2 are in agreement with the ones previously reported (*ca.* −36.3 kJ mol^{-1} on average, in the range 1–2.5 mmol g^{-1}),[8] and in agreement with the average heat of desorption obtained from the GCMC calculations ran in this work (*ca.* 37.0–43.4 kJ mol^{-1} within the same loading range). The increase observed above 2.25 mmol g^{-1} for CO_2 and above 0.75 mmol g^{-1} for CH_4 is due to adsorbate–adsorbate interactions, that become more dominant as loading increases and the available adsorption sites in MIL-120(Al) become gradually occupied (*i.e.*, compression inside the pores). In comparison with other materials (*cf.* Table S10 in the SI), the CO_2 enthalpy of adsorption estimated for MIL-120(Al) is higher than for the reviewed AC,[21–24] CMS,[13,14] the MCM-41 silica,[42] zeolites Silicalite-1,[25] NaY[29] and Na-ZSM-5,[30] and the majority of MOFs[13,20,21,23,43] reviewed, and generally in line with the remaining zeolites[13,25–28] reviewed.

MIL-120(Al) has been further shaped into beads to make it more suitable for continuous operation in industrial biogas upgrading systems like PSA. Millimetre-sized beads have been obtained *via* the wet granulation method using 5% (w/w) bentonite as binder (*cf.* the Experimental section and Fig. S2 in the SI), achieving similar characterisation properties as the powder material (*cf.* Section S1.B in the SI) and similar to the previous study in which a slightly different shaping method had been used.[8] The performance of the shaped form of MIL-120(Al) has also been evaluated. The single-component CO_2 and CH_4 adsorption isotherms at 25 °C, represented in Fig. 2D, are similar to those measured for the powder form of MIL-120(Al), with only a small decrease in adsorption capacity (on average, *ca.* 6% for CH_4 and *ca.* 7% for CO_2), attributed to the presence of a non-porous binder (5% (w/w)) (*cf.* Fig. S3C and Table S1 in the SI). This suggests that the shaping procedure did not impact the overall adsorption properties of the MOF. IAST has also been used to predict the mean selectivity and phase diagrams of the separation of CO_2 and CH_4 at 25 °C, based on a method proposed by Myers[39,40] described in previous works.[15,44] The IAST mean selectivity, represented in Fig. S5 in the SI, shows a similar increase of the mean selectivity with pressure for both materials (shaped and powder). MIL-120(Al) also shows a higher IAST-predicted mean selectivity of CO_2 over CH_4 at 5 bar than other materials reviewed (*cf.* Table S10 in the SI), with the notable exception of two amine-functionalised SBA-15 materials, on which CO_2 is strongly chemisorbed.[16] The IAST-predicted phase diagrams at 5 bar are shown in Fig. S6 in the SI. For the binary mixture of CO_2 and CH_4 at a molar fraction of 0.5 in the gas phase (y_{CH_4}) – the composition of a typical biogas feed[1,2] – the molar fraction of CH_4 in the adsorbed phase (x_{CH_4}) is *ca.* 0.02 for both samples (*cf.* Fig. S6A in the SI). This means that the adsorbed phase is much richer in CO_2 than in CH_4 for both materials, further highlighting the high selectivity of MIL-120(Al) for this separation. The complete phase diagrams in Fig. S6B in the SI further confirm that both materials present a similar performance in terms of selectivity and adsorption capacity of CO_2.

Following these promising results, the adsorption of an equimolar CO_2 : CH_4 gas mixture has been studied under dynamic conditions, by measuring the breakthrough curves at 25 °C and *ca.* 1 bar, in a fixed-bed adsorption system illustrated in Fig. S48 in the SI. Additional experimental details are described in the Experimental section, in Section S2.C in the SI and in a previous work.[24] To evaluate the recyclability of the material, a series of ten consecutive adsorption–desorption cycles have been performed, with a duration of 1 h per cycle (30 min for each adsorption and desorption branch). The ten sets of curves are represented consecutively in Fig. 5 and overlapped in Fig. S49 in the SI. The breakthrough curves confirm that MIL-120(Al) is more selective towards CO_2, as CH_4 breaks through the column ahead of CO_2. The selectivity calculated from breakthrough run 1, *ca.* 89, is higher than for a biomass-based AC,[10] similar to that for benchmark zeolite 13X[21] and lower than that for NH_2-MIL-53(Al)[21] (*cf.* Table S10 in the SI). Additionally, a roll-up of CH_4, indicative of the displacement of

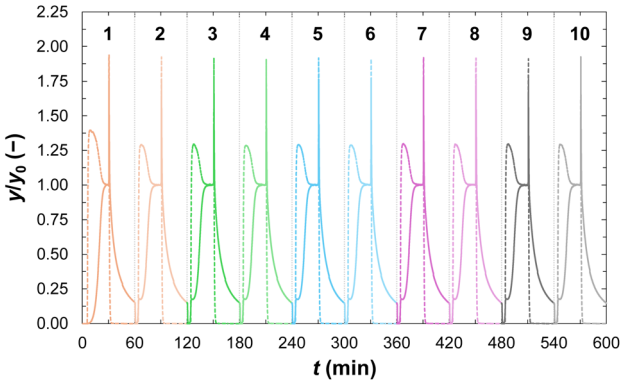

Fig. 5 Consecutive CH_4 (dashed lines) and CO_2 (full lines) breakthrough curves for experimental runs 1 to 10 measured at 25 °C and *ca.* 1 bar for the shaped MIL-120(Al).

the weakly adsorbed CH_4 by CO_2,[45] is also clearly visible in all adsorption branches, further emphasising the higher affinity of the material towards CO_2. The adsorption uptakes calculated from the experimental curves are listed and compared with those predicted from IAST in Table S9 in the SI. The adsorption uptakes calculated from the experimental curves for run 1 for CO_2 are slightly lower but very close to those predicted from IAST, however for CH_4 these differences are higher which can be attributed to both experimental error in the quantification of the low amount of CH_4,[24] and the assumptions of the model. Due to these differences in CH_4 uptake, the selectivities obtained from IAST and breakthrough experiments are different. We recall that IAST values are estimated from the mixture adsorbed amounts in the material, using the experimental data of the pure components' adsorption, which may contribute in part to the observed selectivity differences. Furthermore, considering the GCMC gas mixture isotherms, obtained for a theoretical perfect crystal structure, the selectivity at 1 bar varies between *ca.* 51 for Str1 and *ca.* 201 for Str2. Nevertheless, the overall agreement is a good indicator of the validity of the methodologies and assumptions used. From run 1 to run 2 there is a loss in CO_2 adsorption capacity of *ca.* 35% (*ca.* 1 mmol g^{-1}) that is due to the incomplete regeneration of the material in 30 min. After run 2, the adsorption capacity is maintained throughout the remaining cycles, as seen by the overlapped breakthrough curves and calculated uptakes (*cf.* Fig. S49 and Table S9 in the SI). This shows that the loss in CO_2 adsorption capacity is not cumulative and is only a function of the regeneration conditions, reflecting the reversible nature of the host–guest interactions between CO_2 and the chemical environment inside the pores of the material, namely the hydrogen bonds between CO_2 and the μ_2-OH groups in MIL-120(Al). For CH_4, the weakly adsorbed component in the mixture, 30 min is sufficient time to purge the material of all adsorbed CH_4 and the adsorption capacity is maintained (*cf.* Table S9 in the SI).

Adsorption performance under moisture

The impact of water on the adsorption capacity of MIL-120(Al) has also been studied. Water is an important contaminant in biogas streams and during an adsorption process it can compete for the adsorption sites and significantly reduce the adsorption capacity. While most of the water can be removed during the compression stage of the raw biogas feed, some traces are always present, and its complete removal is very costly. Thus, as a first assessment, a small amount of water vapour (*ca.* 0.16 mmol g^{-1}, corresponding to only traces of water in the gas feed[8]) was pre-adsorbed onto the powder, and the single-component adsorption isotherms of CO_2 and CH_4 were measured at 25 °C. The resulting CO_2 and CH_4 isotherms are compared with the isotherms initially measured under dry conditions in Fig. 6A, and it can be seen that pre-adsorbing *ca.* 0.16 mmol g^{-1} does not affect the adsorption capacity of MIL-120(Al) (in powder form), as both sets of isotherms overlap. This is a clear advantage over some classical zeolites (*e.g.*, 13X) that are very hydrophilic due to the binding of water on the surface cations.

The performance of the shaped material has been tested under humid conditions with an equimolar CO_2 : CH_4 gas mixture at *ca.* 1 bar and 25 °C in the fixed-bed dynamic adsorption system, by pre-loading the material with water vapour in two tests (additional details in the Experimental section and in Section S2.C in the SI). On the first test, a helium (He) flow carrying water vapour at a relative humidity (RH) of 50% was passed through the packed bed for *ca.* 3 h and 30 min, after which the equimolar CO_2 : CH_4 gas mixture was passed

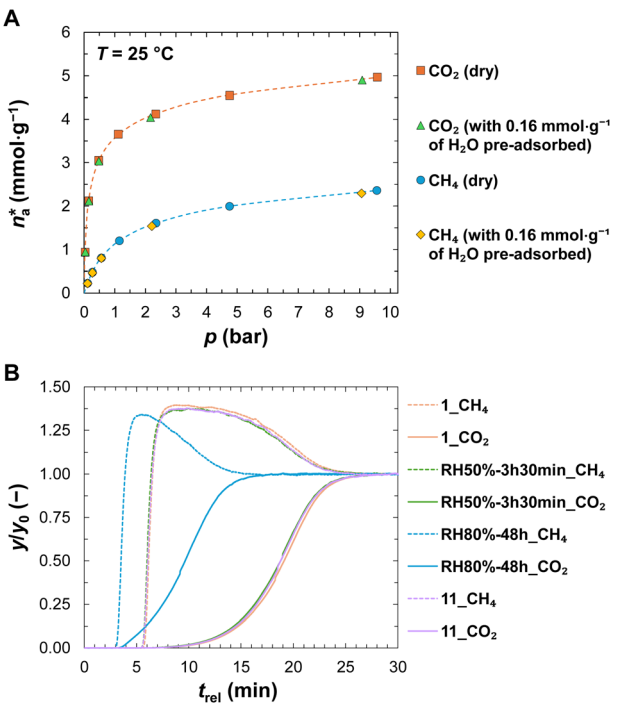

Fig. 6 (A) Single-component adsorption isotherms of CO_2 and CH_4 at 25 °C for MIL-120(Al) (powder form), without and with pre-adsorbed water. (B) Overlap of the adsorption branch of the CO_2 (full lines) and CH_4 (dashed lines) breakthrough curves of experimental runs 1, RH50%-3 h 30 min, RH80%-48 h, and 11, measured at 25 °C and *ca.* 1 bar for the shaped MIL-120(Al). The dashed lines in (A) represent the non-linear least-square fit of the Virial isotherm model to the experimental data (*cf.* Table S3 in the SI).

through the packed bed. The resulting breakthrough curves, illustrated in Fig. 6B, overlap with those of run 1 (performed under dry conditions, *cf.* Fig. 5). With these conditions of %RH and contact time, the material is still not at saturation equilibrium due to the slow water adsorption kinetics, and thus, it does not appear to have any effect on the CO_2 and CH_4 adsorption capabilities of the material. To further understand the effect of the presence of water vapour inside the pores of MIL-120(Al), an additional experiment was run under more severe humid conditions, by flowing He carrying water vapour at RH = 80% for a prolonged period of exposure of 48 h. The higher humidity content of the stream and the much longer exposure time can better ensure the pores inside the material are saturated with water vapour. The equimolar CO_2 : CH_4 breakthrough run performed after this prolonged exposure to water vapour, represented by the blue curves in Fig. 6B, now clearly shows the effect of the presence of water vapour inside the pores. The curves of both gases are shown to break through ahead of the curves of previous runs (*ca.* 2 min and 30 s for CH_4 and 5 min and 30 s for CO_2) and the calculated uptakes are reduced by half for CO_2 and *ca.* ten times for CH_4 (*cf.* Table S9 in the SI). Despite this significant loss in adsorption capacity, the slopes of these and the other breakthrough curves remain the same, which indicates that the presence of even this significantly high amount of water vapour inside the pores does not appear to affect the adsorption kinetics of the gases. Additionally, a final dry breakthrough experiment, run 11, has been performed after this last humid run, and following material activation for 12 h with temperature and He flow (*cf.* Section S2.C in the SI). The results of run 11 have shown that the material has been completely regenerated, as seen by the overlapped breakthrough curves in pink in Fig. 6B and calculated gas uptakes in Table S9 in the SI, demonstrating that the high amount of pre-adsorbed water has not altered permanently the physical and chemical environment inside the pores of MIL-120(Al). This performance of MIL-120(Al) is in clear contrast with the cases of hydrophilic zeolites (with low Si/Al ratios) that are severely affected by the presence of water.[46,47]

Conclusions

The microporous aluminium tetracarboxylate MOF MIL-120(Al) has been successfully synthesised at the kilogram scale, shaped and tested for the separation of CO_2 and CH_4, under dry and humid conditions. The single-component adsorption isotherms measured for CO_2 and CH_4 at 25 °C, on both powdered and shaped forms of MIL-120(Al), have confirmed the great potential of the material for the separation of these gases, both in terms of sorption capacity and high selectivity towards CO_2. Molecular simulation studies suggest a rotation of the μ_2-OH groups in MIL-120(Al), that shifts the material between two different configurations, Str1 to Str2, as pressure increases. To further understand this phenomenon, future work could include *in situ* experimental studies, namely neutron scattering, solid state nuclear magnetic resonance (ssNMR) or extended X-ray absorption fine structure (EXAFS) spectroscopies. The isosteric enthalpies of adsorption for CO_2 in the powdered MIL-120(Al) indicate a consistent affinity for CO_2 molecules. The breakthrough experiments carried out for an equimolar CO_2 : CH_4 gas mixture at 25 °C and *ca.* 1 bar on the shaped material have confirmed MIL-120(Al) to be more selective towards CO_2, as it breaks through the packed column after CH_4, in line with the best sorbents studied so far for this application. Indeed, the selectivity values estimated for an equimolar mixture at *ca.* 5 bar from IAST (*ca.* 31) and from the breakthrough curves at *ca.* 1 bar (*ca.* 89) place MIL-120(Al) clearly above other reported MOFs (except for NH_3-MIL-53, where chemisorption is expected) and in line with the best zeolites, although in MIL-120(Al) the water presence does not permanently impair the adsorption separation as in the case of some zeolites with low Si/Al ratios. The cyclability of the material has also been tested under dry conditions, and a loss in CO_2 adsorption capacity related with the short regeneration time has been observed. However, this loss has not been cumulative, as it has only been observed from the first to the second cycle. The adsorption capacity of CO_2 and CH_4 in the MIL-120(Al) powder remains unaffected by trace exposure to humid conditions. The breakthrough experiments under humid conditions in the shaped material have further revealed that even though a prolonged exposure to water vapour at a high RH (80%) had a significant impact on the adsorption uptake of both gases, the adsorption kinetics appeared unaffected. Furthermore, after complete regeneration, the performance of the material was re-established, showing no permanent damage to its adsorption capabilities after the prolonged exposure to water vapour. In addition to its hydrothermal stability, sustainable, cheap and scalable character, these overall results highlight the great potential of MIL-120(Al) for biogas upgrading. This strongly supports the continuation of further studies to optimise the regeneration conditions and the cyclic separation of biogas, and ascertain the stability of the material in the presence of corrosive gases.

Experimental

Large scale green synthesis of MIL-120(Al) at ambient pressure

Deionised (DI) water (16 litres) was heated to 80 °C in a 30-litre reactor (Fig. S1 in the SI). Once the temperature was reached, 1,2,4,5-benzene-tetracarboxylate (H_4BTeC) (2.13 mol, 542 g) and aluminium acetate, $Al(OH)(OAc)_2 \cdot 1.38H_2O$, (8.57 mol, 1.39 kg) were added. The resulting suspension was heated to 100 °C and stirred at 200 rpm for 24 h. The white crude product was collected by filtration, yielding approximately 1.5 kg of the as-synthesised sample (STY = 60 kg m^{-3} d^{-1}). It was then washed twice with boiling DI water overnight. The washed sample was dried in air.

Shaping of MIL-120(Al) into beads

The MIL-120(Al) powder was shaped into spheres by wet granulation followed by spheronisation: at first, the MOF was mixed with 5% (w/w) of an inorganic binder – bentonite – using a mixer. After that, the powder blend was transferred into the wet granulator bowl and water was added dropwise while

mixing until uniform granules were formed. The wet granules were then fed to the spheroniser with the speed set to 250 rpm for 10 min to obtain spherical beads. The resulting spheres, ranging in diameter, d_p, from 0.5 to 3 mm, were sieved to achieve a more uniform size distribution. Beads selected for experimental measurements were between 1.4 and 2 mm in diameter (Fig. S2 in the SI). The spheres were calcined at 50 °C under vacuum for 12 h.

Characterisation of MIL-120(Al) powder and beads

Powder X-ray diffraction (PXRD) data were collected using a high-throughput Bruker D8 Advance diffractometer working on transmission mode and equipped with a focusing Göbel mirror producing Cu K_α radiation ($\lambda = 1.5418$ Å) and a LynxEye detector. Nitrogen sorption data at 77 K was collected on a Micromeritics Tristar instrument. Prior to the measurement, the sample was degassed at 150 °C using a Micromeritics SmartVacPrep degas unit. Thermogravimetric analysis was conducted using a Mettler Toledo TGA/DSC 2, STAR System apparatus with a heating rate of 5 °C min^{-1} under oxygen flow. Mettler Toledo FiveEasyTM Plus pH mV^{-1} bench meter. Scanning electron microscopy (SEM) micrographs of the MIL-120(Al) powder were captured using a FEI Magellan 400 scanning electron microscope.

Experimental single-component adsorption studies

Single-component adsorption equilibrium isotherms of CO_2 (99.998%, Air Liquide) and CH_4 (99.995%, Air Liquide) were measured for pressures up to 10 bar on MIL-120(Al) in powder form at 25, 35 and 45 °C and on the shaped beads at 25 °C. The gas adsorption isotherms were measured in a lab-made stainless steel volumetric apparatus used in previous works.[17,24,48] The samples were first degassed *in situ* at 150 °C (heating rate of 5 °C min^{-1}) for 8 h, under vacuum in the range of 10^{-9} bar. The experimental isotherms were fit using the Virial isotherm model,[49–52] and binary gas mixture selectivity and phase diagrams were estimated based on IAST,[39] following a method proposed by Myers[40] that is described in detail in previous works.[15,44] The Clausius–Clapeyron equation was used to determine the isosteric enthalpies of adsorption.[41] The experiments performed under humid conditions were run as described in a previous work,[17] with activation *in situ* at 150 °C (heating rate of 5 °C min^{-1}) for 16 h, under vacuum in the range of 10^{-9} bar, before each isotherm measurement. Additional details in Section S2.A in the SI.

Molecular simulation studies

The two crystalline structures considered for MIL-120(Al), Str1 and Str2, were optimised by DFT calculations with VASP,[32–35] version 6.1.2. GCMC calculations[53] were run in RASPA,[31] version 2.0, in both MIL-120(Al) structures to compute single-component (at 25, 35 and 45 °C) and mixture adsorption isotherms (at 25 °C) for pressures up to 10 bar, with partial atomic charges obtained with the REPEAT method.[54] All RASPA runs were computed in a $4 \times 2 \times 5$ simulation box, with 2×10^4 cycles for initialisation followed by 1×10^5 cycles for production. Additional details in Section S2.B in the SI.

Experimental multi-component adsorption studies

Binary breakthrough experiments of CO_2 (99.998%, Air Liquide) and CH_4 (99.995%, Air Liquide) mixtures were conducted on the shaped MIL-120(Al) beads (particle size with d_p [1.4–2] mm) under dry and wet (with pre-adsorbed water vapour) conditions at 25 °C and *ca.* 1 bar, in a lab-made fixed-bed dynamic adsorption system, represented in Fig. S48 in the SI. For the breakthrough experiments under humid conditions, the activated material was initially exposed to a flow of He carrying water vapour at the desired relative humidity, after which the material was exposed to a flow of the dry equimolar CO_2 : CH_4 mixture. Additional details in Section S2.C in the SI.

Author contributions

The manuscript was written through contributions of all authors. All authors have given approval to the final version of the manuscript.

Conflicts of interest

There are no conflicts to declare.

Data availability

The data supporting this article have been included as part of the supplementary information (SI). Supplementary information: characterisation of the materials; detailed description of the experimental and computational adsorption studies; additional experimental and computational results; a comparison with other adsorbent materials. See DOI: https://doi.org/10.1039/d5ta07225e.

Acknowledgements

This research was developed in the scope of the Projects FCT-UIDB/04028/2025 and FCT-UIDP/04028/2025 (CERENA), and UID/50011/2025 with DOI: 10.54499/UID/50011/2025 and LA/P/0006/2020 with DOI: 10.54499/LA/P/0006/2020 (CICECO - Aveiro Institute of Materials), financed by Portuguese funds through FCT/MCTES, and when applicable co-financed by ERDF under the PT2020 Partnership Agreement. M. B. acknowledges FCT for the PhD Grant Reference SFRH/BD/147239/2019. B. C. is grateful for support from a CSC grant (grant number 201804910475). G. M. and C. S. acknowledge the European Union's Horizon 2020 research and innovation program under grant agreement No. 831975 (MOF4AIR project) for providing financial support.

References

1 C. A. Grande, in *Biofuel's Engineering Process Technology*, InTech, 2011, pp. 65–84.

2 L. Paz, S. Gentil, V. Fierro and A. Celzard, *J. Environ. Chem. Eng.*, 2024, **12**, 114870.
3 S. Chaemchuen, N. A. Kabir, K. Zhou and F. Verpoort, *Chem. Soc. Rev.*, 2013, **42**, 9304–9332.
4 A. Khan, M. A. Qyyum, H. Saulat, R. Ahmad, X. S. Peng and M. Lee, *Appl. Mater. Today*, 2021, **22**, 100925.
5 R. Sahoo, S. Mondal, D. Mukherjee and M. C. Das, *Adv. Funct. Mater.*, 2022, **32**, 2207197.
6 D. Chakraborty, A. Yurdusen, G. Mouchaham, F. Nouar and C. Serre, *Adv. Funct. Mater.*, 2024, **34**, 1–23.
7 C. Volkringer, T. Loiseau, M. Haouas, F. Taulelle, D. Popov, M. Burghammer, C. Riekel, C. Zlotea, F. Cuevas, M. Latroche, D. Phanon, C. Knöfelv, P. L. Llewellyn and G. Férey, *Chem. Mater.*, 2009, **21**, 5783–5791.
8 B. Chen, D. Fan, R. V. Pinto, I. Dovgaliuk, S. Nandi, D. Chakraborty, N. García-Moncada, A. Vimont, C. J. McMonagle, M. Bordonhos, A. Al Mohtar, I. Cornu, P. Florian, N. Heymans, M. Daturi, G. De Weireld, M. Pinto, F. Nouar, G. Maurin, G. Mouchaham and C. Serre, *Adv. Sci.*, 2024, **11**, 2401070.
9 C. A. Grande, R. Blom, A. Möller and J. Möllmer, *Chem. Eng. Sci.*, 2013, **89**, 10–20.
10 I. Durán, N. Álvarez-Gutiérrez, F. Rubiera and C. Pevida, *Chem. Eng. J.*, 2018, **353**, 197–207.
11 N. Álvarez-Gutiérrez, M. V. Gil, F. Rubiera and C. Pevida, *Fuel Process. Technol.*, 2016, **142**, 361–369.
12 N. Álvarez-Gutiérrez, S. García, M. V. Gil, F. Rubiera and C. Pevida, *Energy Fuels*, 2016, **30**, 5005–5015.
13 A. D. Wiersum, J. S. Chang, C. Serre and P. L. Llewellyn, *Langmuir*, 2013, **29**, 3301–3309.
14 X. Song, L. Wang, X. Ma and Y. Zeng, *Appl. Surf. Sci.*, 2017, **396**, 870–878.
15 J. Pires, V. K. Saini and M. L. Pinto, *Environ. Sci. Technol.*, 2008, **42**, 8727–8732.
16 L. Mafra, T. Čendak, S. Schneider, P. V. Wiper, J. Pires, J. R. B. Gomes and M. L. Pinto, *Chem. Eng. J.*, 2018, **336**, 612–621.
17 M. Pacheco, M. Bordonhos, M. Sardo, R. Afonso, J. R. B. Gomes, L. Mafra and M. L. Pinto, *Chem. Eng. J.*, 2022, **443**, 136271.
18 Y. Belmabkhout and A. Sayari, *Chem. Eng. Sci.*, 2009, **64**, 3729–3735.
19 M. A. O. Lourenço, C. Siquet, M. Sardo, L. Mafra, J. Pires, M. Jorge, M. L. Pinto, P. Ferreira and J. R. B. Gomes, *J. Phys. Chem.*, 2016, **120**, 3863–3875.
20 N. Singh, S. Dalakoti, A. Sharma, R. Chauhan, R. S. Murali, S. Divekar, S. Dasgupta and Aarti, *Sep. Purif. Technol.*, 2024, **341**, 012072.
21 S. A. Peter, G. V. Baron, J. Gascon, F. Kapteijn and J. F. M. Denayer, *Adsorption*, 2013, **19**, 1235–1244.
22 A. D. Wiersum, C. Giovannangeli, D. Vincent, E. Bloch, H. Reinsch, N. Stock, J. S. Lee, J. S. Chang and P. L. Llewellyn, *ACS Comb. Sci.*, 2013, **15**, 111–119.
23 H. N. Wamba, S. Dalakoti, N. Singh, S. Divekar, J. Ngoune, A. Arya and S. Dasgupta, *Ind. Eng. Chem. Res.*, 2023, **62**, 19773–19783.
24 M. Bordonhos, M. I. S. Neves, A. Marandi, F. Nouar, M. Jorge, J. R. B. Gomes, C. Serre and M. L. Pinto, *Chem. Eng. J.*, 2025, **524**, 169276.
25 J. Yang, J. Li, W. Wang, L. Li and J. Li, *Ind. Eng. Chem. Res.*, 2013, **52**, 17856–17864.
26 S. Cavenati, C. A. Grande and A. E. Rodrigues, *J. Chem. Eng. Data*, 2004, **49**, 1095–1101.
27 K. G. Wynnyk, B. Hojjati, P. Pirzadeh and R. A. Marriott, *Adsorption*, 2017, **23**, 149–162.
28 M. Mofarahi and F. Gholipour, *Microporous Mesoporous Mater.*, 2014, **200**, 1–10.
29 A. Sharma, A. Verma, U. Kumar, N. Singh, S. Dalakoti, R. Chauhan, S. Bhandari, S. Divekar, S. Dasgupta and Aarti, *Microporous Mesoporous Mater.*, 2024, **367**, 112984.
30 M. Rahmani, B. Mokhtarani, M. Mafi and N. Rahmanian, *Ind. Eng. Chem. Res.*, 2022, **61**, 6600–6610.
31 D. Dubbeldam, S. Calero, D. E. Ellis and R. Q. Snurr, *Mol. Simul.*, 2015, **42**, 81–101.
32 G. Kresse and J. Hafner, *Phys. Rev. B:Condens. Matter Mater. Phys.*, 1993, **47**, 558–561.
33 G. Kresse and J. Hafner, *Phys. Rev. B:Condens. Matter Mater. Phys.*, 1994, **49**, 14251–14269.
34 G. Kresse and J. Furthmüller, *Comput. Mater. Sci.*, 1996, **6**, 15–50.
35 G. Kresse and J. Furthmüller, *Phys. Rev. B:Condens. Matter Mater. Phys.*, 1996, **54**, 11169–11186.
36 W. Humphrey, A. Dalke and K. Schulten, *J. Mol. Graphics*, 1996, **14**, 33–38.
37 X. Jin, Y. Li, K. Gaedecke, X. Zhang and B. Smit, *ChemRxiv*, 2025, preprint, DOI: 10.26434/chemrxiv-2025-dqdkf.
38 D. Fan, F. L. Oliveira, M. Wahiduzzaman and G. Maurin, *arXiv*, 2025, preprint, arXiv:2508.20608, DOI: 10.48550/arXiv.2508.20608.
39 A. L. Myers and J. M. Prausnitz, *AIChE J.*, 1965, **11**, 121–127.
40 A. L. Myers, *Adsorption*, 2003, **9**, 9–16.
41 A. Nuhnen and C. Janiak, *Dalton Trans.*, 2020, **49**, 10295–10307.
42 Y. Belmabkhout, R. Serna-Guerrero and A. Sayari, *Chem. Eng. Sci.*, 2009, **64**, 3721–3728.
43 D. Damasceno Borges, P. Normand, A. Permiakova, R. Babarao, N. Heymans, D. S. Galvao, C. Serre, G. De Weireld and G. Maurin, *J. Phys. Chem. C*, 2017, **121**, 26822–26832.
44 M. L. Pinto, J. Pires and J. Rocha, *J. Phys. Chem. C*, 2008, **112**, 14394–14402.
45 N. S. Wilkins, A. Rajendran and S. Farooq, *Adsorption*, 2021, **27**, 397–422.
46 J. M. Kolle, M. Fayaz and A. Sayari, *Chem. Rev.*, 2021, **121**, 7280–7345.
47 D. G. Boer, J. Langerak and P. P. Pescarmona, *ACS Appl. Energy Mater.*, 2023, **6**, 2634–2656.
48 M. Bordonhos, M. Lourenço, J. R. B. Gomes, P. Ferreira and M. L. Pinto, *Microporous Mesoporous Mater.*, 2021, **317**, 110975.
49 D. M. Ruthven, *Principles of Adsorption and Adsorption Processes*, John Wiley & Sons, 1984.
50 F. J. Wilkins, *Proc. R. Soc. London, Ser. A*, 1938, **164**, 496–509.

51 R. M. Barrer and R. M. Gibbons, *Trans. Faraday Soc.*, 1963, **59**, 2875–2887.
52 A. V. Kiselev, *J. Colloid Interface Sci.*, 1968, **28**, 430–442.
53 D. Dubbeldam, A. Torres-Knoop and K. S. Walton, *Mol. Simul.*, 2013, **39**, 1253–1292.
54 C. Campañá, B. Mussard and T. K. Woo, *J. Chem. Theory Comput.*, 2009, **5**, 2866–2878.